

# Tunable Photoconduction Sensitivity and Bandwidth for Lithographically Patterned Nanocrystalline Cadmium Selenide Nanowires

Sheng-Chin Kung,<sup>†</sup> Wendong Xing,<sup>†</sup> Wytze E. van der Veer,<sup>†</sup> Fan Yang,<sup>†</sup> Keith C. Donavan,<sup>†</sup> Ming Cheng,<sup>†</sup> John C. Hemminger,<sup>†</sup> and Reginald M. Penner<sup>†,‡,\*</sup>

<sup>†</sup>Department of Chemistry, University of California, Irvine, California 92697-2025, United States, and <sup>‡</sup>Department of Chemical Engineering and Materials Science, University of California, Irvine, California 92697-2700, United States

The properties of nanowire photoconductors have been studied since 2002 when Yang and co-workers first observed photoconduction in individual single-crystalline nanowires composed of zinc oxide ( $ZnO$ )<sup>1</sup> and tin dioxide ( $SnO_2$ ).<sup>2</sup> In those experiments, and in subsequent work involving nanowires of  $ZnO$ ,<sup>3–10</sup>  $SnO_2$ ,<sup>11,12</sup> gallium nitride ( $GaN$ ),<sup>13–15</sup> and cadmium sulfide ( $CdS$ ),<sup>16–19</sup> there have been two surprises: First, the photoconductive gain can be orders of magnitude higher for nanowires than for single crystalline thin films of the same material,<sup>13,20,21</sup> and second, the photocurrent rise and decay times, extending to seconds for some nanowire systems, are often orders of magnitude slower.<sup>13,20,21</sup> It has been suggested<sup>13,20</sup> that these two disparities between films and nanowires derive from the same phenomenon: the existence of a barrier for electron–hole recombination caused by a surface electric field. Depending upon the material, the source of this electric field is the trapping of electrons or holes at surface states in the case of cadmium sulfide ( $CdS$ )<sup>19</sup> and cadmium selenide ( $CdSe$ ),<sup>22</sup> the reaction of holes with ambient  $O_2$  for oxide nanowires,<sup>6,20,23</sup> or in the case of  $GaN$ , by Fermi level pinning, which is itself caused by surface hole trapping.<sup>13,21</sup> For single crystalline nanowires, several degrees of freedom provide for the possibility of tunability of the photoconductivity performance metrics. These are the nanowire diameter, the crystallographic orientation of its long axis, the dopant density, and the chemical termination of wire surfaces. However we are aware of just two studies in which the influence of any of these parameters on the photoconductivity

**ABSTRACT** Nanocrystalline cadmium selenide ( $nc\text{-}CdSe$ ) nanowires were prepared using the lithographically patterned nanowire electrodeposition method. Arrays of 350 linear  $nc\text{-}CdSe$  nanowires with lateral dimensions of  $60\text{ nm (h)} \times 200\text{ nm (w)}$  were patterned at  $5\text{ }\mu\text{m}$  pitch on glass.  $nc\text{-}CdSe$  nanowires electrodeposited from aqueous solutions at  $25\text{ }^\circ\text{C}$  had a mean grain diameter,  $d_{ave}$ , of 5 nm. A combination of three methods was used to increase  $d_{ave}$  to 10, 20, and 100 nm: (1) The deposition bath was heated to  $75\text{ }^\circ\text{C}$ , (2) nanowires were thermally annealed at  $300\text{ }^\circ\text{C}$ , and (3) nanowires were exposed to methanolic  $CdCl_2$  followed by thermal annealing at  $300\text{ }^\circ\text{C}$ . The morphology, chemical composition, grain diameter, and photoconductivity of the resulting nanowires were studied as a function of  $d_{ave}$ . As  $d_{ave}$  was increased from 10 to 100 nm, the photoconductivity response of the nanowires was modified in two ways: First, the measured photoconductive gain,  $G$ , was elevated from  $G = 0.017$  ( $d_{ave} = 5\text{ nm}$ ) to  $\sim 4.9$  (100 nm), a factor of 290. Second, the photocurrent rise time was increased from  $8\text{ }\mu\text{s}$  for  $d_{ave} = 10\text{ nm}$  to 8 s for 100 nm, corresponding to a decrease by a factor of 1 million of the photoconduction bandwidth from 44 kHz to 44 mHz.

**KEYWORDS:** photodetector · photolithography · electrodeposition · grain diameter · polycrystalline · thermal annealing

properties of nanowires has been investigated. Lüth and co-workers<sup>13</sup> studied the diameter dependence of the photoconductivity for  $GaN$  nanowires, concluding that the aforementioned surface electric field was reduced for nanowires with diameters below 100 nm, reducing the photoconductive gain and accelerating recovery to the dark conductivity following exposure to light as compared with larger nanowires. Wu *et al.*<sup>24</sup> increased the photoconductive gain of single crystalline  $CdS$  nanowires by 3 orders of magnitude by doping these nanowires with chlorine.

Polycrystalline nanowires add one additional degree of freedom: the mean grain diameter,  $d_{ave}$ . In this paper, we explore the possibility of tuning the photoconductive gain and the response/recovery time for

\* Address correspondence to mpenner@uci.edu.

Received for review July 19, 2011 and accepted August 23, 2011.

Published online August 23, 2011  
10.1021/nn202728f

© 2011 American Chemical Society

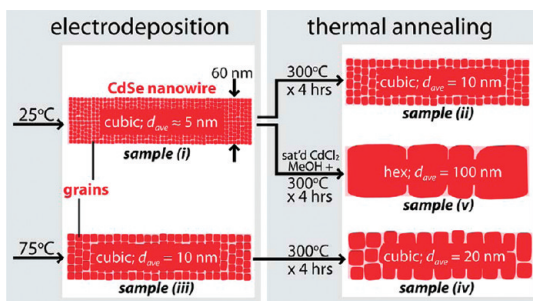


**Figure 1.** Preparation of five polycrystalline *nc*-CdSe nanowires,  $60\text{ nm} \times 200\text{ nm}$  (shown schematically in cross-section), using electrodeposition and thermal annealing.

nanocrystalline CdSe nanowires by adjusting  $d_{\text{ave}}$ . Recently,<sup>25</sup> we have demonstrated that nanocrystalline CdSe (*nc*-CdSe) nanowires with  $d_{\text{ave}} \approx 10\text{ nm}$  can be prepared using the lithographically patterned nanowire electrodeposition (LPNE) method.<sup>26–28</sup> These nanowires exhibit a photoconduction bandwidth approaching 45 kHz, among the highest observed in any type of nanowire to date, but the photoconductive gain was just 0.032–0.050, among the lowest values reported for semiconductor nanowires of any type.<sup>25</sup> Here, we start with arrays of  $d_{\text{ave}} \approx 5\text{ nm}$  *nc*-CdSe nanowires having dimensions of  $60\text{ nm} \times 200\text{ nm}$ , and we use three processes to increase  $d_{\text{ave}}$  (Figure 1): (1) electrodeposition from hot plating solution ( $75\text{ }^{\circ}\text{C}$ ), (2) post-deposition thermal annealing at  $300\text{ }^{\circ}\text{C}$  for 4 h, and (3) postdeposition exposure to methanolic  $\text{CdCl}_2$  followed by thermal annealing as in (2).  $\text{CdCl}_2$  has been used as a chlorine dopant source for photoconductive CdSe films since the 1970s,<sup>29</sup> and its ability to facilitate grain growth in cadmium telluride (CdTe) and CdSe has been established.<sup>30–32</sup> Recently, Cl doping has also been associated with enhancement of photoconductive gain in single crystalline CdS nanowires.<sup>24</sup> Using a combination of these three methods, *nc*-CdSe nanowires with  $d_{\text{ave}}$  values of 10, 20, and 100 nm were obtained without altering the lateral dimensions of the nanowire.

The influence of grain diameter on photoconductivity performance has not been probed previously for polycrystalline nanowires to our knowledge, and there is a paucity of data even for semiconductor thin films. Nair *et al.*<sup>33</sup> prepared X-ray amorphous CdSe films by chemical bath deposition and studied the photoconductivity of these films as a function of the thermal annealing temperature and duration. The photosensitivity,  $S = (\sigma_{\text{photo}} - \sigma_{\text{dark}})/\sigma_{\text{dark}}$ , was elevated from  $S = 10$ , for unannealed films, to  $10^7$  for wurtzite-phase films heated for 20–40 min at  $450\text{ }^{\circ}\text{C}$  in air. This increase in  $S$  was correlated with the incorporation of oxygen into the CdSe matrix, but the grain diameter and its evolution with annealing conditions were not reported.<sup>33</sup> Yoneda *et al.*<sup>34</sup> reported an investigation of the photoconductivity properties of CVD diamond films over the

range  $10\text{ }\mu\text{m} > d_{\text{ave}} > 0.1\text{ }\mu\text{m}$ . Photocurrent decay times were observed to decrease with  $d_{\text{ave}}$  over this range from 80 to 40 ps.<sup>34</sup> Chakrabarti *et al.*<sup>35</sup> prepared evaporated CdTe films with mean grain diameters ranging from 60 to 200 nm and reported that these films exhibit an anomalous decrease in carrier mobility with increasing grain diameter over this range. The grain diameter-dependent photoconductivity, however, was not reported in that work.<sup>35</sup> Gosh *et al.*<sup>36</sup> reported an enhancement in the photosensitivity of polycrystalline ZnO films as the mean grain diameter was increased from 64 to 135 nm.

## RESULTS AND DISCUSSION

**Synthesis of *nc*-CdSe Nanowires Using LPNE.** Recently,<sup>25</sup> we described the synthesis of *nc*-CdSe nanowires using the LPNE process in conjunction with the scanning electrodeposition stripping method.<sup>37–40</sup> Near-stoichiometric CdSe nanowires were obtained by using an asymmetrical aqueous plating solution containing 0.30 M  $\text{CdSO}_4$ , 0.70 mM  $\text{SeO}_2$ , and 0.25 M  $\text{H}_2\text{SO}_4$  at pH 1–2.<sup>41,42</sup> Cathodic deposition from this solution at  $25\text{ }^{\circ}\text{C}$  results in the deposition of CdSe as well as elemental Cd and Se (Figure 2a, top two traces). But by using a skewed Cd:Se ratio of 43:1, the quantity of excess Se is minimized. Then, excess elemental Cd is removed from the nascent CdSe nanowires by scanning the deposition potential over a potential range encompassing both CdSe cathodic electrodeposition and Cd anodic stripping (Figure 2a, bottom trace). Heating the plating solution to  $75\text{ }^{\circ}\text{C}$  increases the cathodic current associated with the deposition processes as well as the Cd stripping current (Figure 2b). Scanning electron microscopy (SEM) examination of the nanowires produced at both temperatures (Figure 2c) shows that these nanowires have a compact, quasi-rectangular cross-section and a width that increases linearly with the number of deposition/stripping cycles (Figure 2d). At  $25\text{ }^{\circ}\text{C}$ , each deposition/stripping cycle adds 9.4 nm to the width of the nanowire; at  $75\text{ }^{\circ}\text{C}$ , each cycle adds 35 nm. Atomic force microscopy (AFM) images (Figure 2e,f) show a patterned array of CdSe nanowires on glass (Figure 2e). At higher magnification (Figure 2f) the quasi-rectangular cross-section of each nanowire is apparent. For the photoconductivity investigations described next, *nc*-CdSe nanowires deposited at  $25\text{ }^{\circ}\text{C}$  were prepared using 20 scans and were  $238\text{ }(\pm 7)\text{ nm}$  in width, whereas those deposited at  $75\text{ }^{\circ}\text{C}$  were prepared using 3 scans and were  $181\text{ }(\pm 7)\text{ nm}$  in width.

**GIXRD, TEM, and SEM Characterization of As-Deposited and Annealed *nc*-CdSe Nanowires.** Grazing incidence X-ray diffraction measurements were carried out on lithographically patterned arrays of thousands of nanowires deposited at  $5\text{ }\mu\text{m}$  pitch on glass (Figure 3), and transmission electron microscopy (TEM) images (Figure 4) were acquired on nanowires that were removed from the

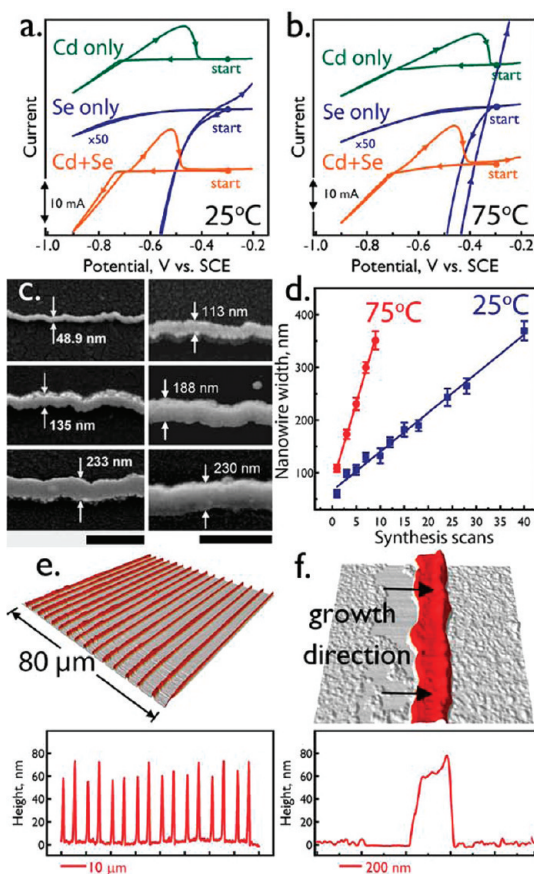


**Figure 2.** (a) Cyclic voltammograms at 50 mV/s and 25 °C for LPNE-patterned templates in three different solutions: “Cd only” (green), aqueous  $[Cd^{2+}] = 0.30\text{ M}$ ,  $H_2SO_4 = 0.25\text{ M}$ , pH = 1–2; “Se only” (blue), aqueous  $[HSeO_2^+] = 0.70\text{ mM}$ ,  $[H_2SO_4] = 0.25\text{ M}$ , and “Cd+Se” (orange),  $[Cd^{2+}] = 0.30\text{ M}$ ,  $[HSeO_2^+] = 0.70\text{ mM}$ , and  $[H_2SO_4] = 0.25\text{ M}$ . (b) Same experiment as (a) at 75 °C. (c) Scanning electron micrographs (SEM) of nc-CdSe nanowires prepared using 1, 10, and 24 synthesis scans at 25 °C (left, top to bottom) and 1, 3, and 5 synthesis scans at 75 °C (right, top to bottom). Scale bar = 500 nm. (d) Plot of mean nanowire width versus the number of synthesis scans for depositions carried out at 25 °C (blue) and 75 °C (red). (e, f) Atomic force micrographs (AFM) of nc-CdSe nanowires. Amplitude traces acquired for each image are shown below.

photoresist-coated glass surface by exposure to acetone and transferred to copper grids. A histogram of grain diameters can be constructed by acquiring TEM images of the same nanowire section at a series of tilt angles relative to the electron beam axis. In each of these images, a unique subset of the grains meets the condition for diffraction of the electron beam, and these grains appear black in the brightfield transmission image,<sup>43</sup> facilitating the accurate measurement of grain diameters. The mean grain diameters of nc-CdSe nanowires estimated using these two methods (Table 1) were similar but not identical. It is important to appreciate that GIXRD and TEM provide complementary information: the GIXRD measurement probes the nanowire structure close to the surface normal, corresponding to the smallest, 60 nm vertical dimension of these

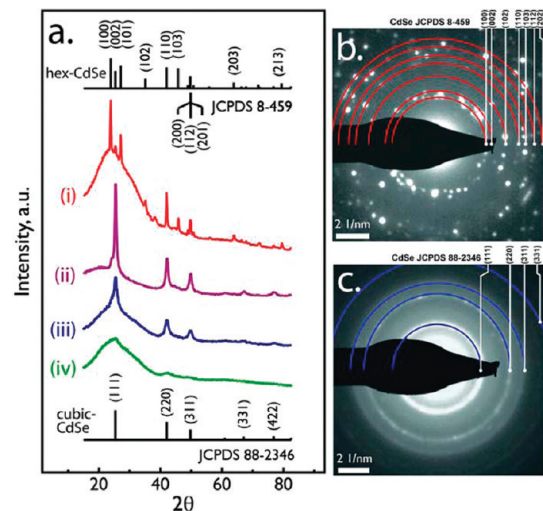


**Figure 3.** (a) Grazing incidence ( $\Omega = 0.3^\circ$ ) X-ray diffraction pattern (GIXRD) for arrays of nc-CdSe nanowires deposited with 5  $\mu\text{m}$  spacing on glass: (i) deposited at 25 °C, dipped in saturated  $CdCl_2/CH_3OH$  solution, and annealed ( $N_2$ , 300 °C, 4 h), (ii) deposited at 75 °C and annealed ( $N_2$ , 300 °C, 4 h), (iii) deposited at 75 °C; (iv) as-deposited at 25 °C. A broad reflection centered at  $\sim 25^\circ$  in each pattern is derived from the amorphous glass surface. (b, c) Selected area electron diffraction patterns for (b) sample (i) and (c) sample (iii) showing the same principle reflections seen for these samples by XRD. The discontinuous diffraction rings seen in (b) are a consequence of the large grain dimensions in this sample.

nanowires, whereas TEM images the grain structure orthogonal to this, within the 200 nm lateral dimension and along the nanowire axis. In addition, nc-CdSe nanowires prepared for TEM analysis were all 20 nm in height to enable transmission of the electron beam. Grain size data for GIXRD and TEM are summarized in Table 1 for five samples. nc-CdSe nanowires deposited at 25 °C are X-ray amorphous (Figure 3a, trace (iv)), but transmission electron micrographs of these wires (Figure 4d) show some crystalline grains approximately 5 nm in diameter. Increasing the deposition temperature to 75 °C increases the crystallinity of nc-CdSe nanowires, and three reflections assigned to zinc blende are then observed by GIXRD for these samples (Figure 3a, trace (iii)). The line-width of the (111) reflection was used to estimate the grain diameter using the Scherrer equation:<sup>44</sup>

$$d_{ave} = 0.89 \frac{\lambda}{B \cos \theta} \quad (1)$$

where  $d_{ave}$  is the mean grain diameter,  $\lambda$  is the X-ray wavelength,  $B$  is the full width of the peak measured at half-height, and  $\theta$  is the diffraction angle.  $d_{ave} \approx 10\text{ nm}$  is obtained for nc-CdSe nanowires prepared from 75 °C solution. The same degree of grain growth was obtained by electrodepositing at 25 °C and then thermally annealing in flowing  $N_2$  at 300 °C for 4 h (Figure 3a, trace (ii) and Figure 4c). When the same thermal annealing program was applied to nc-CdSe nanowires

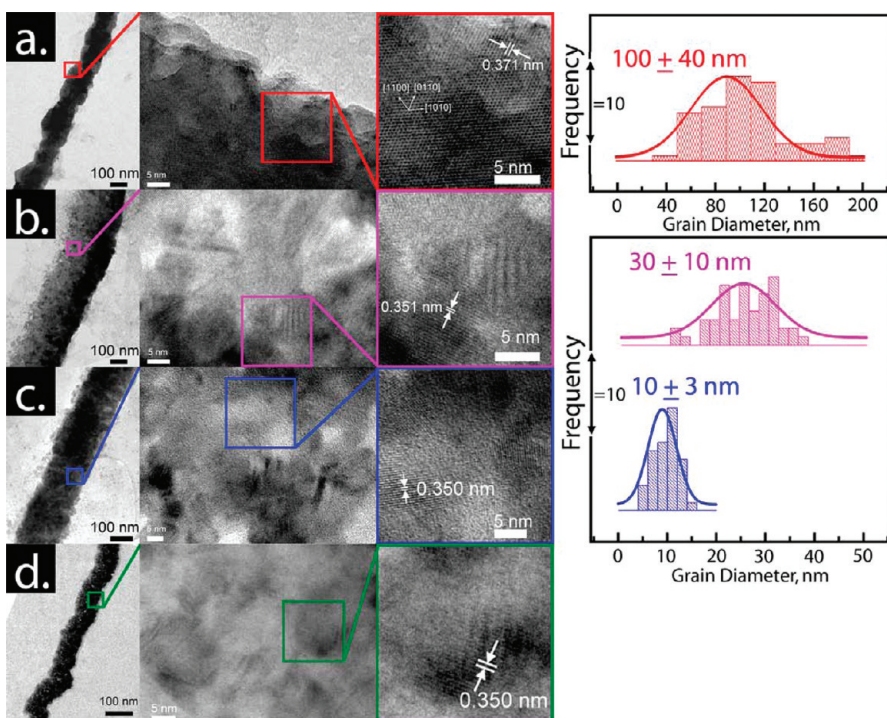


**Figure 4.** Transmission electron micrographs at progressively higher magnification of the same CdSe nanowires analyzed by XRD in Figure 2: (a) deposited at 25 °C, dipped in a saturated CdCl<sub>2</sub>/CH<sub>3</sub>OH solution, and annealed (N<sub>2</sub>, 300 °C, 4 h), (b) deposited at 75 °C and annealed (N<sub>2</sub>, 300 °C, 4 h), (c) deposited at 75 °C, (d) as-deposited at 25 °C. At right are shown histograms of the grain diameter determined using tilt-resolved bright-field TEM image sequences.

**TABLE 1. Summary of Preparation Conditions, Average Grain Diameters, and Electrical Resistivities for nc-CdSe Nanowires**

sample	preparation conditions	d <sub>ave</sub> (nm)			
		GIXRD <sup>a</sup>	TEM <sup>b</sup>	crystal structure <sup>c</sup>	resistivity (Ωcm)
(i)	T <sub>dep</sub> = 25 °C	n.a.	4.9 ± 0.5	cubic	(6.4 ± 0.2) × 10 <sup>5</sup>
(ii)	T <sub>dep</sub> = 25 °C; 300 °C × 4 h, N <sub>2</sub>	11 ± 1	10 ± 3	cubic	(5.4 ± 0.2) × 10 <sup>5</sup>
(iii)	T <sub>dep</sub> = 75 °C	11 ± 1	10 ± 3	cubic	same as (ii)
(iv)	T <sub>dep</sub> = 75 °C; 300 °C × 4 h, N <sub>2</sub>	15 ± 1	30 ± 10	cubic	(1.0 ± 0.2) × 10 <sup>5</sup>
(v)	T <sub>dep</sub> = 25 °C; sat'd CdCl <sub>2</sub> , MeOH, 5 s 300 °C × 4 h, N <sub>2</sub>	29 ± 2	100 ± 40	hexagonal	(7.6 ± 0.3) × 10 <sup>5</sup>

<sup>a</sup> GIXRD = grazing incidence X-ray diffraction; the average grain diameter was determined by broadening of the (111) reflection, for cubic wires, and (100), for hexagonal wires, using the Scherrer equation, eq 1. <sup>b</sup> TEM = transmission electron microscopy; the average grain diameter was determined by direct measurement of crystallites along [111].

<sup>c</sup> cubic = zinc blende; hexagonal = wurtzite.

prepared from 75 °C, d<sub>ave</sub> increased to ~20 nm (Figure 3a, trace (ii) and Figure 4b). Finally, following a procedure described in many previous papers,<sup>30–32</sup> we dipped nc-CdSe nanowires prepared from 25 °C in saturated, methanolic CdCl<sub>2</sub> for 5 s and then annealed using the same program described above. This procedure produced more rapid grain growth with d<sub>ave</sub> increasing to 100 nm (Figure 3a, trace (i) and Figure 4a). In addition, a phase transition from zinc blende to wurtzite is also observed (Figure 3a, trace (i)). This phase transition has been reported to occur in CdSe nanostructures and thin films at temperatures near 300 °C,<sup>45–49</sup> much lower than the temperature required to induce this phase transition in bulk CdSe (>1000 °C).<sup>46</sup>

TEM analysis confirms the crystallographic assignments made by GIXRD. A lattice-resolved image for a nanowire deposited at 25 °C, for example (Figure 4d), reveals the lattice planes separated by 3.50 Å consistent with the spacing of (111) planes in zinc blende CdSe. On the other hand, the morphology of nc-CdSe nanowires processed by dipping in methanolic CdCl<sub>2</sub> prior to thermal annealing shows much larger grains (Figure 4a). The characteristic hexagonal lattice directions including [1̄100], [01̄10], and [10̄10] can be indexed to wurtzite phase CdSe in a high-resolution TEM image (Figure 4a, right). In that image, the interplane distance is slightly expanded from the cubic value (0.35 Å) to 3.71 Å, in agreement with the (100) plane spacing of hexagonal CdSe.

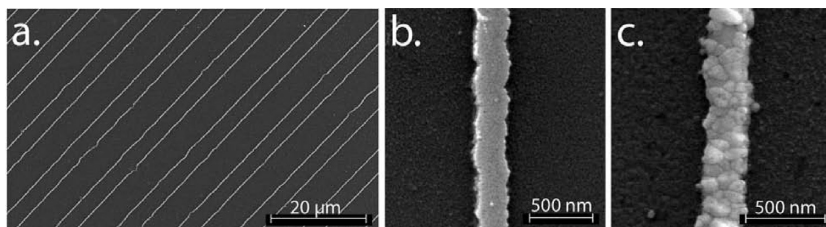


**Figure 5.** Scanning electron microscopy (SEM) images of (a) an array of *nc*-CdSe nanowires and, at higher magnification, (b) *nc*-CdSe nanowires processed without and (c) with exposure to methanolic  $\text{CdCl}_2$ .

*nc*-CdSe nanowires were also examined by scanning electron microscopy. Linear nanowire arrays patterned at 5  $\mu\text{m}$  pitch were used for this purpose (Figure 5a). At higher magnification, no observable changes to the morphology of *nc*-CdSe nanowires were induced either by electrodepositing from 75 °C solution, by thermal annealing in flowing  $\text{N}_2$  at 300 °C for 4 h, or by application of both treatments (Figure 5b). But samples that were exposed first to  $\text{CdCl}_2$  and then annealed exhibited a roughened surface texture in which individual 30–190 nm grains were clearly discernible at the wire surface (Figure 5c). The wire width and mean height, however, were retained to within  $\pm 20\%$  in spite of this grain growth and attendant surface roughening.

**X-ray Photoelectron Spectroscopy (XPS) Analysis.** XPS was used to probe the surface chemical composition of *nc*-CdSe nanowire arrays and to determine the extent to which chlorine incorporation occurs for nanowires of sample (v) that were treated with  $\text{CdCl}_2$ . XPS spectra for *nc*-CdSe nanowires were identical for all samples that were not exposed to  $\text{CdCl}_2$  solution ((−) $\text{CdCl}_2$ ); so in Figure 6, we show spectra for these samples together with spectra of (+) $\text{CdCl}_2$  nanowire samples: those that were treated with  $\text{CdCl}_2$  in methanol. In both types of samples, the Cd 3d spectral region (Figure 6a) is characterized by two spin-orbit components with binding energies of 405.8 and 411.7 eV, associated with Cd (3d<sub>5/2</sub>) and Cd (3d<sub>3/2</sub>), respectively. Just one chemical state is seen for Cd on these samples, and the measured binding energy is within 0.5 eV of that reported earlier for CdSe.<sup>50</sup> CdO, with a Cd 3d binding energy of 404.2 eV,<sup>50</sup> would be easily detected by XPS if it were present at concentrations greater than 10% of a monolayer, but we did not observe peaks at this lower energy. Like the Cd 3d region, the Se 3d spectral region (Figure 6b) consists of an envelope containing both Se 3d<sub>5/2</sub> and Se 3d<sub>3/2</sub> photoemission lines at 53.9 and 53.1 eV, respectively, on the basis of Gaussian deconvolution peak fitting. Again, these spectra are consistent with the presence of a single chemical state for Se at the surfaces of (−) $\text{CdCl}_2$  and (+) $\text{CdCl}_2$  CdSe nanowires, and these binding energies are within 0.2 eV of those reported previously for Se in CdSe,<sup>51,52</sup> while they are ∼0.80 eV lower than the binding energy for selenium in either  $\text{SeO}_2$  or  $\text{H}_2\text{SeO}_3$ . The absence of peaks near 60 eV indicates an absence of significant

$\text{SeO}_x$ .<sup>53</sup> Thus, on the basis of XPS analysis of the Cd and Se spectral regions the data show that the crystalline bulk CdSe of the nanowire is terminated at nanowire surfaces without significant formation of other compounds, including oxides of either Cd or Se.

We determined the atomic sensitivity ratios for Cd 3d and Se 3d photoelectrons by analyzing a freshly cleaved single crystal of CdSe. These data permit the surface Cd:Se stoichiometry of *nc*-CdSe nanowires to be determined. (−) $\text{CdCl}_2$  nanowire surfaces were close to stoichiometric with Cd:Se = 1.08, whereas the surfaces of (+) $\text{CdCl}_2$  nanowires were slightly cadmium-rich: Cd:Se = 1.48.

XPS was also used to assess whether significant chlorine was present on the surfaces of (+) $\text{CdCl}_2$  nanowires and within the bulk of these nanowires. The surfaces of (−) $\text{CdCl}_2$  nanowire are free of XPS-detectable Cl (Figure 6c), but the Cl 2p spectrum of (+) $\text{CdCl}_2$  nanowires shows a strong spin-orbit doublet for Cl with the more intense Cl 2p<sub>3/2</sub> component at 198.4 eV (Cl 2p<sub>3/2</sub>), close to the expected binding energy for Cl in this compound.<sup>54</sup> The intensity of the Cl signal is undiminished as the nanowire surface is gradually removed by  $\text{Ar}^+$  sputtering for 2 and 10 min (Figure 6d). This suggests that chlorine is incorporated at approximately uniform concentration throughout the nanowire cross-section. The thickness of CdSe removed by  $\text{Ar}^+$  sputtering was determined by measuring the mean nanowire height by AFM before (Figure 6e) and after (Figure 6f) sputtering for 10 min, a difference of ∼5 nm. Thus, the photoconductivity results reported below must be interpreted in terms of the presence of Cl dopant within (+) $\text{CdCl}_2$  *nc*-CdSe nanowires.

**Photoconduction in *nc*-CdSe Nanowires.** How does grain growth in *nc*-CdSe nanowires influence optical and photoconductivity properties? Differences between the optical absorption and photoluminescence spectra among the four types of nanowires we prepared, corresponding to four different  $d_{\text{ave}}$  values ranging from 5 to 100 nm (Table 1), are imperceptible. Optical absorption spectra for these arrays are weak, owing to the low areal density of nanowires deposited on the glass surface, corresponding to a coverage of just 4% for nanowires 200 nm in width, but absorption onsets near the expected bandgap for CdSe of 1.75 eV were observed for all samples (Figure 7a,d). All four samples

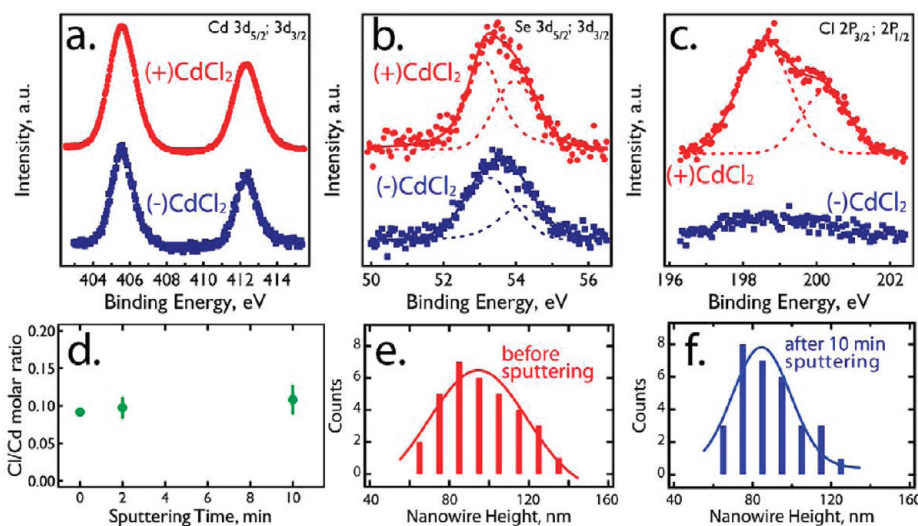


**Figure 6.** X-ray photoelectron spectra (XPS) of *nc*-CdSe nanowire arrays patterned at 5  $\mu\text{m}$  pitch on glass without ((−)CdCl<sub>2</sub>) and with ((+)CdCl<sub>2</sub>) treatment with methanolic CdCl<sub>2</sub>: (a) Cd 3d spectral region, (b) Se 3d spectral region, (c) Cl 2p spectral region. The dashed lines in (b) and (c) show the results of Gaussian deconvolution. (d) Plot of chlorine:cadmium ratio for ((+)CdCl<sub>2</sub>) nanowires as a function of the Ar<sup>+</sup> sputtering time. (e, f) Histograms of nanowire height measured using AFM for ((+)CdCl<sub>2</sub>) nanowires before (e) and after (f) 10 min of Ar<sup>+</sup> sputtering. Approximately 5 nm of the nanowire surface is removed by this process.

also showed strong, band-edge photoluminescence centered at energies of 1.74–1.76 eV with no observable red-shifted trap state emission (Figure 7a,d).

The photoconductivity of arrays of 350 *nc*-CdSe nanowires, deposited at 5  $\mu\text{m}$  pitch on glass, were probed in this study. In our photocurrent spectrometer (Figure 8a), a chopped 532 nm laser beam was directed onto these nanowire arrays, which were shielded in a Faraday cage from stray electrical noise. Arrays of nanowires rather than single nanowires were studied because we found that the high electrical resistance of single nanowires produced currents in the 10<sup>−10</sup>–10<sup>−12</sup> A range, severely limiting the available measurement bandwidth. Thus for single nanowires, the intrinsic photocurrent rise and decay behavior could not be observed. Amplifying the current for a single nanowire by 350, however, increases the available bandwidth by the same factor and renders the gain bandwidth of our measurement circuit sufficient to measure microsecond photocurrent transients with high signal-to-noise ratio (see below). Lengths of 5  $\mu\text{m}$  of these nanowires were electrically contacted by evaporated gold electrodes with a thickness of 40 nm (Figure 8b,c), and a 2 V bias was applied across this gap for all measurements unless otherwise indicated.

Whereas the absorption and photoluminescence spectra were similar for all four of the samples investigated here, dramatic differences were observed in the photoconductivity properties of these nanowires. If, for example, the nanowires of sample (ii) (cubic;  $d_{\text{ave}} = 10$  nm) are compared with those of sample (v) (hexagonal;  $d_{\text{ave}} = 100$  nm), the photocurrent amplitude at any incident light intensity is larger for sample (v) by a factor of 200 (Figure 7c,f) and the onset of the

photocurrent with increasing photon energy is also more abrupt (Figure 7b,e). The gradual photocurrent onset observed for sample (ii) above the bandgap is attributed to the electronic heterogeneity of the ~10 nm grains present in this material, mediated in part by quantum-confined and blue-shifted absorption edges for the smallest grains within it (Figure 4c). Conversely, the rapid increase in photocurrent observed for sample (v) suggests that little electronic heterogeneity exists between the ~100 nm diameter grains within this nanowire. A common feature of the two photosensitivity traces is the decay in photocurrent amplitude for photon energies above ~2.3 eV. This behavior has been frequently observed in the spectral response for nanowires<sup>16,22,55</sup> and films<sup>56</sup> of cadmium chalcogenides as well as for other materials.<sup>36</sup> Because the absorption coefficient increases monotonically with increasing photon energy,<sup>57</sup> photoexcited carriers are produced in closer proximity to the surface of the absorber and the surface traps inevitably present there, reducing the carrier lifetime and diminishing the photocurrent.<sup>58</sup> These differences suggest that  $d_{\text{ave}}$  is a parameter that exerts considerable influence over the photoconductivity performance of these nanowires, and in what follows, we probe the influence of  $d_{\text{ave}}$  on the transient properties of the photocurrent and on the photocurrent amplitude.

The photocurrent amplitude for the four samples of interest here (Figure 9a–d) increases by almost 3 orders of magnitude with increasing grain diameter from  $d_{\text{ave}} \approx 5$  nm (sample (i), Figure 9a) to  $d_{\text{ave}} \approx 100$  nm (sample (v), Figure 9d). Three metrics are commonly used to quantitate the sensitivity of photoconductors to light: The photosensitivity,  $S$  (defined above),

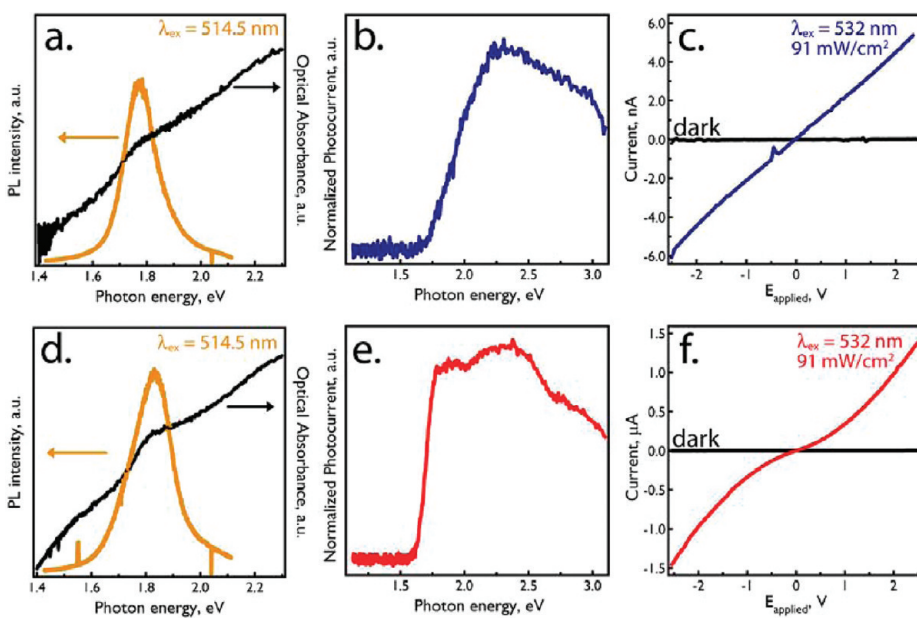


**Figure 7.** Optical and photoconductivity properties of 350 nc-CdSe nanowire arrays on glass. (a–c) Data for (−)CdCl<sub>2</sub> nanowires, corresponding to sample (ii) in Table 1. (d–f) Data for (+)CdCl<sub>2</sub> nanowires of sample (v). (a, d) Absorption spectra and photoluminescence spectra acquired with excitation at 514.5 nm. (b, e) Photocurrent spectral response for  $E_{\text{bias}} = 1.0$  V, using a chopped (135 Hz) illumination (with a power of 1.2 mW/cm<sup>2</sup> at 500 nm). (c, f) Current versus voltage traces measured in the dark and with illumination at 532 nm, 91 mW/cm<sup>2</sup>.

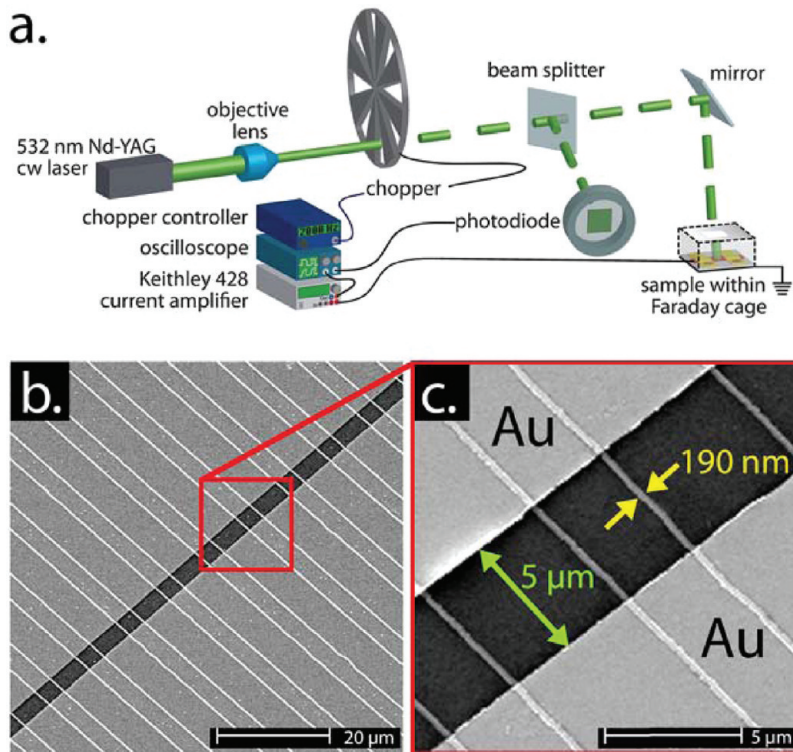


**Figure 8.** (a) Schematic diagram showing the apparatus employed for measuring the photoconductivity properties of nc-CdSe nanowires. (b) Scanning electron microscope (SEM) image showing part of an ensemble of 350 nc-CdSe nanowires bridging evaporated gold electrodes configured with a 5  $\mu\text{m}$  spacing. (c) Five nanowires within this device are shown at higher magnification.

the gain,  $G$ , and the responsivity,  $R$ .  $S$  quantitates the fractional change in the conductivity at the

illuminated photoconductor referenced to the dark photoconductor:<sup>58</sup> The gain,  $G$ , is the number of

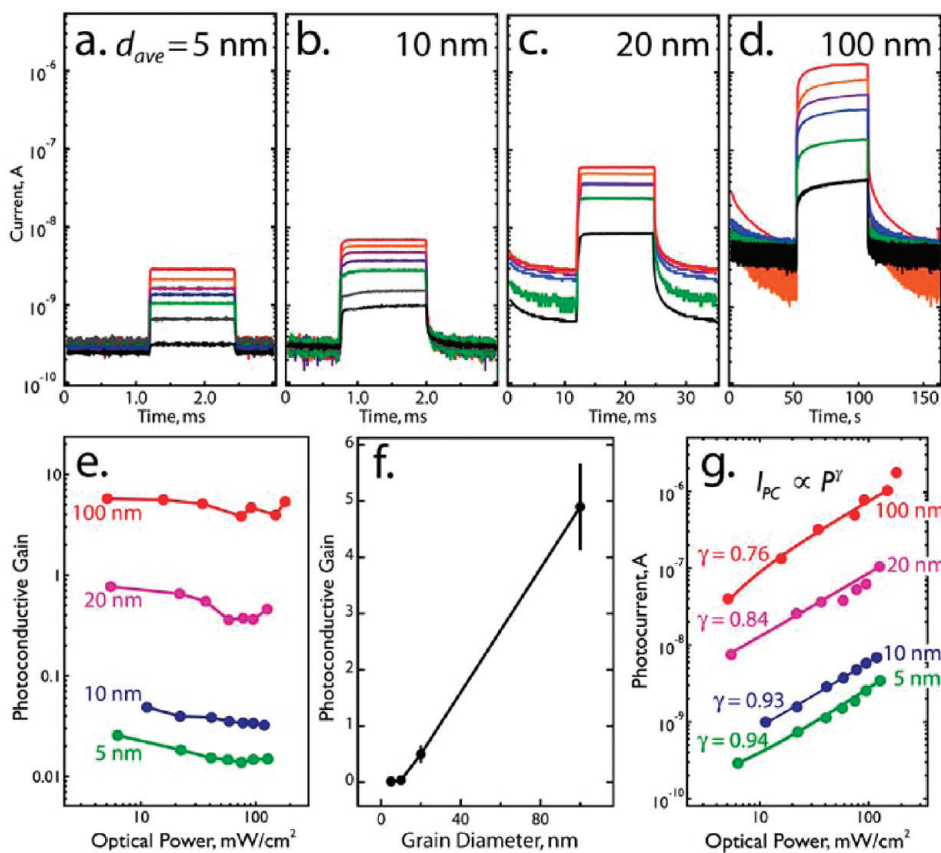


**Figure 9.** (a–d) Optical power dependence of the photocurrent for four *nc*-CdSe nanowire arrays with  $d_{ave}$  as indicated. The range of optical powers plotted here are (a) 6.3 to 128  $\text{mV/cm}^2$ , (b) 11 to 119  $\text{mV/cm}^2$ , (c) 5.5 to 95  $\text{mV/cm}^2$ , and (d) 5.5 to 181  $\text{mV/cm}^2$ . (e) Plot of  $G$  versus  $P_{\text{optical}}$ . In this calculation, it is assumed that 80% of the incident photons are absorbed and that 90% of the 350 nanowires present in each device are electrically continuous. (f) Plot of  $G$  versus  $d_{ave}$ . (g) Correlation between the generated photocurrent and incident optical power of 350  $\times$  *nc*-CdSe nanowires, plotted as the best fit to a simple power law:  $i_{\text{photo}} \propto P_{\text{optical}}^\gamma$ .

electrons produced in the external circuit for each absorbed photon:<sup>58</sup>

$$G = \frac{\tau}{\tau_{\text{tr}}} = \frac{\mu\tau V}{l^2} \quad (2)$$

where  $\tau$  is the lifetime of photoexcited carriers,  $\tau_{\text{tr}}$  is the transit time for carriers between the two contacts,  $\mu$  is the carrier mobility,  $V$  is the applied voltage, and  $l$  is the distance between contacts. Equivalently,  $G$  can be defined in terms of the steady-state photocurrent,  $I_{\text{photo}}$ , and the optical power,  $P_{\text{optical}}$ , as follows:

$$G = \frac{I_{\text{photo}}}{q} \frac{h\nu}{P_{\text{optical}}} \frac{1}{\eta^* N w l} \quad (3)$$

where  $h$  is Planck's constant,  $\nu$  is the frequency,  $q$  is the elementary charge,  $\eta^*$  is the effective photocarrier generation efficiency (including the effects of reflection, scattering, and incomplete absorption, taken to be 0.8),  $(w l)$  is the area of a single nanowire, and  $N$  is the number of nanowires, taken to be 315 in the present case (90% of 350).  $R$  (units: A/W) is the photocurrent normalized by the incident optical

power on the nanowires:<sup>58</sup>

$$R = \frac{I_{\text{photo}}}{P_{\text{optical}} N w l} = \frac{G \eta^*}{(h\nu/q)} = \frac{G \eta^* \lambda(\text{nm})}{1240} \quad (4)$$

where  $\lambda$  (nm) is the wavelength of the incident illumination.

For the *nc*-CdSe nanowires investigated here, all three of these metrics increase with  $d_{ave}$  across the range  $d_{ave}$  from 5 to 100 nm (Figure 9e,f and Table 2):  $G$  and  $R$  both increase by a factor of 290, while  $S$ , which depends upon the incident optical power, increases by a factor of 375 for  $P = 91 \text{ mW/cm}^2$ .  $G$  and  $R$ , which depend exclusively on the properties of the illuminated photoconductor, are both proportional to  $\mu\tau$ . Although we have not measured  $\mu$  in this study, the influence of  $d_{ave}$  on  $\mu$  has been intensively investigated for polycrystalline semiconductor thin films, and it has been demonstrated<sup>59,60</sup> that  $\mu \propto d_{ave}$ .  $\tau$ , on the other hand, can be approximated by the time necessary for photoinduced charge carriers to encounter a grain boundary. If it can be assumed that carrier recombination is a diffusive process that

**TABLE 2. Summary of Photoconductivity Metrics for nc-CdSe Nanowires**

sample(s)	$d_{\text{ave}}/\text{cryst struct}$	photocurrent amplitude			transient response		
		$S^a$	$G^b$	$R^c$ (A/W)	$\tau_{\text{resp}}^d$ (μs)	$\tau_{\text{rec,fast}}^e$ (μs)	$\tau_{\text{rec,slow}}^f$ (μs)
(i)	~5 nm cubic	8 ± 2	0.017 ± 0.004	0.0058 ± 0.002	49 ± 5	17 ± 1	42 ± 3
(ii), (iii)	10 nm cubic	20 ± 2	0.037 ± 0.005	0.013 ± 0.002	8 ± 2	3 ± 1	30 ± 7
(iv)	20 nm cubic	10 ± 1	0.5 ± 0.2	0.17 ± 0.07	200 ± 70	230 ± 70	$6(±1) \times 10^3$
(v)	100 nm hex	300 ± 100	4.9 ± 0.8	1.7 ± 0.3	$(8 ± 2) \times 10^6$	$(1.7 ± 0.2) \times 10^3$	$(2.7 ± 0.9) \times 10^6$

<sup>a</sup>  $S$  = photosensitivity. The  $P_{\text{optical}} = 95 \text{ mW/cm}^2$  except for sample (v) where  $P_{\text{optical}} = 91 \text{ mW/cm}^2$ . <sup>b</sup>  $G$  = photoconductive gain at 532 nm, from eq 3, averaged over optical powers from 5 to 103 mW/cm<sup>2</sup>. <sup>c</sup>  $R$  = responsivity at 532 nm, from eq 4 assuming  $\eta^* = 0.80$ , averaged over optical powers from 5 to 103 mW/cm<sup>2</sup>. <sup>d</sup> Response time. <sup>e</sup> Recovery time for the fast component of the photocurrent relaxation. <sup>f</sup> Recovery time for the slow component of the photocurrent relaxation.

occurs efficiently at grain boundaries, then<sup>57</sup>

$$\tau \approx \frac{q(d_{\text{ave}})^2}{kT\mu} \quad (5)$$

So to first-order, as  $d_{\text{ave}}$  is increased from 5 to 100 nm, a factor of 20, we expect  $\mu\tau$  and therefore  $G$  and  $R$  to increase by  $20 \times 20 = 400$ , whereas a factor of 290 is seen experimentally. It should be noted here that chlorine incorporation into single crystalline CdS nanowires has been associated<sup>24</sup> with 1000-fold increases in  $G$ , so there is every reason to expect the presence of chlorine in the nc-CdSe nanowires of sample (v) to be a second factor, together with  $d_{\text{ave}}$ , contributing to the elevation of  $G$ .

In prior work going back more than 50 years,<sup>61,62</sup> the optical power dependence of the photocurrent has often been observed to conform to the equation

$$I_{\text{photo}} \propto P_{\text{optical}}^\gamma \quad (6)$$

where  $0.5 < \gamma < 1.0$ . For nc-CdSe nanowires the measured optical power dependence of the photocurrent also adheres to eq 6 with  $\gamma$  decreasing monotonically with increasing  $d_{\text{ave}}$  from 0.94 ( $d_{\text{ave}} = 5 \text{ nm}$ ) to 0.76 ( $d_{\text{ave}} = 100 \text{ nm}$ ) (Figure 9g). In prior work,<sup>22</sup> single crystalline CdSe nanoribbons were characterized by a  $\gamma$  value at 600 nm of 0.77, nearly identical to the value we observe for sample (v). The canonical treatment of noninteger  $\gamma$  values is that of Rose,<sup>61</sup> who considered the influence of electron trap states arrayed in the energy interval between the conduction band edge and mid band gap and encompassing the Fermi level,  $E_F$ . Within this model, a  $\gamma$  value of 1.0 is obtained for a uniform, energy-independent, density of trap states that are filled (by photoexcitation) below  $E_F$  and empty above it.<sup>61,62</sup> If instead a preponderance of these states are filled above  $E_F$ , then  $\gamma = 0.5$  is observed. Noninteger  $\gamma$  values are associated with a nonuniform state distribution. In particular, Rose proposed<sup>61</sup> that the state density decreases exponentially with energy below the conduction band edge, and the validity of this state distribution for Cd(SSe) sintered films, chemically similar to the nc-CdSe nanowires, was later confirmed.<sup>63</sup> The exact noninteger value of  $\gamma$  then depends upon

where  $E_F$  is located within this exponential distribution relative to the level of trap filling.<sup>62</sup> When interpreted using the Rose model, our data supports the existence of a quasi-uniform trap state distribution for  $d_{\text{ave}} = 5 \text{ nm}$  nanowires, filled below  $E_F$  ( $\gamma = 0.94$ ), and the observed decrease in  $\gamma$  indicates that this distribution deviates from uniformity, becoming progressively more exponential with increasing  $d_{\text{ave}}$ . If the transformation from a uniform trap state distribution to an exponentially distributed distribution occurs via the loss of deep trap states, then the data of Figure 9g can be reconciled, at least qualitatively, with the increase in  $G$  (Figure 9e) and the decrease in response/recovery times (see below) that occur in parallel as  $d_{\text{ave}}$  increases from sample (i) to sample (v).

The transformation from sample (i) with  $G = 0.017$  to sample (v) with  $G = 4.9$  creates nc-CdSe nanowires with an optical photosensitivity,  $S$ , that is comparable to that seen for the CdSe and CdTe nanowires studied previously, including single crystalline nanowires. Fan *et al.*<sup>64</sup> studied arrays of ~2000 single crystalline CdSe nanowires and reported  $S \approx 40$  ( $P_{\text{optical}} = 4.4 \text{ mW/cm}^2$  white light,  $V = 2 \text{ V}$ ), whereas we measured  $S \approx 10$  for sample (v) under similar illumination conditions ( $P_{\text{optical}} = 5 \text{ mW/cm}^2$ ,  $\lambda = 532 \text{ nm}$ ,  $V = 2 \text{ V}$ ). Pena *et al.*<sup>42</sup> reported  $S \approx 15$  for single polycrystalline CdSe nanowires at an unspecified optical power and  $V = 10 \text{ V}$ . Arrays of an unspecified number of single crystalline CdTe nanorods prepared by Wang *et al.*<sup>65</sup> yielded  $S \approx 5–20$  at  $V = 1.5 \text{ V}$  and unspecified illumination conditions. The electrically isolated wire length was reported in none of these previous studies as far as we can tell, so the electrical field strength associated with these measurements of  $S$  is not known.

The increased  $G$  induced by thermal annealing and exposure to  $\text{CdCl}_2$  is obtained at the cost of dramatically slower photocurrent response and recovery (Figure 10). Photocurrent response at  $\lambda = 532 \text{ nm}$  and  $91 \text{ mW/cm}^2$  conformed to a single exponential (Figure 10a–c):

$$I_{\text{photo}} = I_{\text{photo},0}[1 - \exp(-t/\tau_{\text{resp}})] \quad (7)$$

where  $I_{\text{photo},0}$  is the maximum photocurrent,  $t$  is the time, and  $\tau_{\text{resp}}$  is the time constant. Photocurrent recovery in the dark, however, showed two discrete exponential

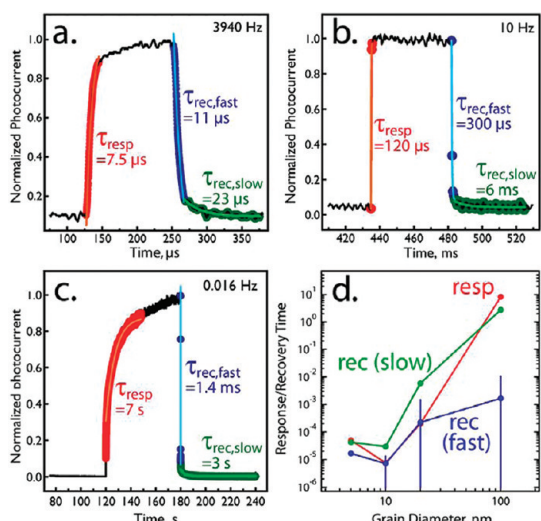


**Figure 10.** (a–c) Normalized photocurrent versus time for 350 *nc*-CdSe nanowire arrays, biased at 2 V. (a) Sample (ii);  $d_{\text{ave}} = 10 \text{ nm}$ . (b) Sample (iv);  $d_{\text{ave}} = 20 \text{ nm}$ . (c) Sample (v);  $d_{\text{ave}} = 100 \text{ nm}$ . (d) Plot of  $\tau_{\text{resp}}$ ,  $\tau_{\text{rec,fast}}$ , and  $\tau_{\text{rec,slow}}$  as a function of  $d_{\text{ave}}$ .

decays for all samples and was therefore fit to a biexponential (Figure 10a–c):

$$I_{\text{photo}} = I_{\text{photo},0} [\exp(-t/\tau_{\text{rec,fast}}) + \exp(-t/\tau_{\text{rec,slow}})] \quad (8)$$

where  $\tau_{\text{rec,fast}}$  and  $\tau_{\text{rec,slow}}$  are the time constants for the fast and slow components of the photocurrent decay, respectively. These three time constants,  $\tau_{\text{resp}}$ ,  $\tau_{\text{rec,fast}}$ , and  $\tau_{\text{rec,slow}}$  are tabulated in Table 2 and plotted in Figure 9d. The observation of two time constants for the photocurrent decay is consistent with a  $\beta$ -type photoconductivity system<sup>66</sup> in which the faster time constant is associated with the recombination of free (untrapped) photo-carriers and the slower one is associated with carrier untrapping. For such systems,  $\tau_{\text{rec,fast}}$  approximately equals the minority carrier lifetime.<sup>57</sup> An increase in  $d_{\text{ave}}$  by a factor of 20 across our samples is correlated with an increase of  $\tau_{\text{rec,fast}}$  by a factor of 560. Our five samples can be classified according to the apparent rate-limiting process for photocurrent response: For samples (ii), (iii), and (iv),  $\tau_{\text{resp}} = \tau_{\text{rec,fast}}$  within the experimental error of our measurement. This behavior is observed if the trapping rate exceeds the rate of free photo carrier recombination while untrapping is significantly slower. For these samples, a time-independent photocurrent is achieved on the time scale of the minority lifetime. For samples (i) and (v) in contrast,  $\tau_{\text{resp}} \approx \tau_{\text{rec,slow}}$ , and this

suggests that the rate-limiting process for photocurrent response is trap filling. For sample (v), the disparity between  $\tau_{\text{rec,slow}}$  and  $\tau_{\text{rec,fast}}$  is more than 3 orders of magnitude. Thus, slow trap filling is likely responsible for the enormous range of response times—a factor of  $10^5$ – $10^6$ —observed for the *nc*-CdSe nanowires examined in this study.

## CONCLUSIONS

We have demonstrated that the LPNE method can be adapted to synthesize single-phase, cubic nanocrystalline CdSe nanowires on glass surfaces. These *nc*-CdSe nanowires have a rectangular cross-section with height and width dimensions that are independently adjustable, down to minimum values of 20 and 50 nm, respectively. The mean grain diameter,  $d_{\text{ave}}$ , of these *nc*-CdSe nanowires can be increased from 5 nm, the value obtained for nanowires electrodeposited at room temperature, to 10, 20, or 100 nm using a combination of thermal annealing, deposition from hot (75 °C) plating solution, and exposure to methanolic CdCl<sub>2</sub>. XPS depth profiling shows that for *nc*-CdSe nanowires exposed to methanolic CdCl<sub>2</sub> before thermal annealing, chlorine is present at a uniform concentration throughout the bulk of the nanowire.

*nc*-CdSe nanowires synthesized at 25 °C and annealed at 300 °C for 4 h have a  $d_{\text{ave}} \approx 10 \text{ nm}$ . Arrays of 350 such nanowires show rapid photocurrent response and recovery characterized by time constants of 8 and 30  $\mu\text{s}$ , respectively. The photoconductive gain of these samples, however, is just 0.037.<sup>25</sup> Increasing  $d_{\text{ave}}$  from 5 to 100 nm increases the photosensitivity by a factor of 375 (for  $P_{\text{optical}} = 91 \text{ mW/cm}^2$ ). The photoconductive gain and the responsivity are both increased by a factor of 290 over this same range of  $d_{\text{ave}}$ . For  $G$  and  $R$ , the magnitude of this increase is consistent with the expected increase in the product ( $\mu\tau$ ) with  $d_{\text{ave}}$ . Response times increase by a much larger factor of  $10^5$ – $10^6$  as  $d_{\text{ave}}$  increases from 5 to 100 nm, a disparity that we attribute to slow trap filling for the  $d_{\text{ave}} = 100 \text{ nm}$  sample (sample (v)).

Collectively, these data show that the critical photoconductive properties of nanowires can be adjusted over a wide range using the mean grain diameter. More work is necessary to fully characterize the energy and number density of the traps present in these nanowires and to learn how the carrier mobility varies with wire dimensions and  $d_{\text{ave}}$ .

## EXPERIMENTAL SECTION

**Chemicals and Materials.** Cadmium sulfate (CdSO<sub>4</sub>·8H<sub>2</sub>O, 98+%), cadmium chloride hemipentahydrate (3CdCl<sub>2</sub>·2.5H<sub>2</sub>O, 98+%), and selenium oxide (SeO<sub>2</sub>, 99.9+%) were used as received from Sigma-Aldrich. Sulfuric acid (ULTREX ultrapure) was purchased from J. T. Baker. Acetone, methanol, and nitric acid were used as

received from Fisher (ACS Certified). Positive photoresists, Shipley S-1808 and S-1827, and developer MF-319 were purchased from Microchem Corporation. Nickel wire and gold pellets (5N purity) were purchased from ESPI Metals.

**CdSe Nanowire Synthesis.** CdSe nanowire arrays were prepared by electrodeposition using the LPNE process.<sup>25–27,67</sup> Nickel

films (ESPI, 5N purity) 20–60 nm in thickness were thermally evaporated onto precleaned 1 in. × 1 in. squares of soda lime glass. A positive photoresist (PR) layer (Shipley, S1808) was spin coated (2500 rpm, 80 s), and a PR layer of ~800 nm thickness was formed after soft-baking (90 °C, 30 min). The PR was then patterned using a contact mask in conjunction with a UV light source equipped with a photolithographic alignment fixture (Newport, 83210i-line, 365 nm × 1.80 s). The exposed PR region was developed for 25 s (Shipley, MF-319), rinsed with Millipore water (Milli-Q,  $\rho > 18 \text{ M}\Omega \cdot \text{cm}$ ), and air-dried. Exposed nickel was removed by dipping the patterned samples in 0.8 M HNO<sub>3</sub> (Fisher, ACS Certified) solution for 6 min to create a horizontal trench with a typical width of 500 nm and a height that equaled the thickness of the evaporated nickel layer. The entire lithographically patterned region was then immersed in an aqueous plating solution with the exception of one edge where an electrical contact to the nickel layer was established with an alligator clip. CdSe nanowires were then electrodeposited in the lithographically produced trench using the scanning electro-deposition/stripping method.<sup>38–40,68</sup> The potential of the nickel edge was scanned at 50 mV/s from an initial potential of –400 mV vs SCE to a negative scan limit of –800 mV and back. The width of the nascent CdSe nanowire was dictated by the number of complete voltammetric scans ranging from 50 nm (1 scan at 25 °C) to 350 nm (40 scans). Two different bath temperatures were employed, 25 and 75 °C, and the deposition rate at 75 °C was much more rapid (Figure 2d). The aqueous plating solution was unstirred aqueous 0.30 M CdSO<sub>4</sub>, 0.70 mM SeO<sub>2</sub>, and 0.25 M H<sub>2</sub>SO<sub>4</sub> at pH 1–2.<sup>37,41,42</sup> (Caution: both CdSO<sub>4</sub> and SeO<sub>2</sub> are highly toxic.) Electrodeposition was conducted using a one-compartment three-electrode electrochemical cell using a Gamry G300 potentiostat. After the CdSe electrodeposition was complete, the remaining PR was removed by rinsing with acetone (Fisher, ACS Certified) and Milli-Q water, and the remaining nickel was removed by soaking in a 0.8 M HNO<sub>3</sub> solution for 10 min. This process produced an array of CdSe nanowires that strongly adhered to the surface of the glass substrate.

Two postdeposition thermal treatments were carried out: (1) As-deposited CdSe nanowires were heated in flowing N<sub>2</sub> at 300 °C for 4 h using a tube furnace (Lindberg, 54233) and then cooled to room temperature. (2) As-deposited CdSe nanowires were dipped in a saturated CdCl<sub>2</sub>/CH<sub>3</sub>OH solution<sup>30–32,69</sup> for 5 s and then thermally annealed as described in (1). After thermal annealing, these CdSe nanowires were rinsed with Milli-Q water to remove residual CdCl<sub>2</sub>.

**Structural Characterization.** Scanning electron micrographs were acquired by using a Philips XL-30 FEGSEM (field emission gun scanning electron microscope) operated at 10 keV. All samples were sputtered with a thin layer of Au/Pd before imaging to prevent charging.

Transmission electron microscopy images and selective area electron diffraction (SAED) patterns were obtained using a Philips CM 20 TEM operating at 200 keV. The as-synthesized CdSe nanowires were released from a PR precoated surface using an acetone stream and then transferred onto a holey carbon film coated Cu grid (Ted Pella, Inc.), as previously described.<sup>67</sup> For the postannealed CdSe nanowires, an aluminum layer evaporated (140 nm) and then thermally oxidized in air at 300 °C for 4 h was executed prior to the LPNE nanowire fabrication. After postannealing, the CdSe nanowires were released from the aluminum oxide layer by dissolving in aqueous 2 M NaOH and then transferred onto the Cu grid and dried overnight before TEM analysis.

Atomic force microscopy images and amplitude traces were acquired using an Asylum Research MFP-3D AFM equipped with Olympus AC160TS tips in a laboratory air ambient.

Grazing-incidence X-ray diffraction patterns were obtained using a Rigaku Ultima III high-resolution X-ray diffractometer employing parallel beam optics with a fixed incident angle of 0.3°. The X-ray generator was operated at 40 kV and 44 mA with Cu K $\alpha$  irradiation. JADE 7.0 (Materials Data, Inc.) X-ray pattern data processing software was used to analyze acquired patterns and estimate the respective grain diameter size.

**X-ray Photoelectron Spectroscopy.** XPS measurements were performed with an ESCALAB MKII (VG Scientific) surface analysis

instrument. The ultra-high-vacuum multichamber system is equipped with a twin anode X-ray source (Mg/Al) and a 150 mm hemispherical electron energy analyzer. Spectra presented here were collected using Mg K $\alpha$  X-rays (1253.6 eV) in constant energy mode with pass energy of 20 eV. During acquisition the base pressure of the spectroscopy chamber was 1 nTorr. XPS peak areas of Cd(3d) and Se(3d) were measured following a standard Shirley background subtraction. Binding energies were calibrated using the C(1s) peak of adventitious carbon set at 284.8 eV as a reference.<sup>53</sup> Deconvolution and spectral line fitting were carried out using XPSPeak 4.1. Ar ion beam sputtering (2 keV) was used for depth profile analysis.

**Optical Properties.** Absorption spectra were recorded from 900 to 400 nm using a UV-vis-NIR photospectrometer (Perkin-Elmer Lambda 900) equipped with an integrating sphere (Lab Sphere Inc.). Photoluminescence spectra were acquired using excitation from a continuous wave argon ion laser (Coherent Innova 90,  $\lambda_{\text{ex}} = 514 \text{ nm}$ , 60 mW). Emission was collected at a normal incidence through a 20× Zeiss EpiPlan microscope objective and then coupled with an f4 lens into an imaging spectrograph (Chromex 250IS), equipped with 300 grooves/mm holographic grating (500 nm blaze) that dispersed light onto a liquid nitrogen cooled CCD (Princeton Instruments, LN/1024EUV) with 1024 × 256 pixels. Signals from the 256 pixels arrayed perpendicular to the long axis of the CCD were binned, producing a linear detector with 1024 channels. Collection times were 60 s.

**Photoconductivity.** Evaporated gold electrical contacts (thickness = 40 nm) with a spacing of 5  $\mu\text{m}$  were photolithographically patterned on top of an array of 350 nc-CdSe nanowires, and a 1.0 V bias was applied. The spectral response of the photocurrent was acquired using a photocurrent spectrometer consisting of a 75 W xenon arc lamp (Oriel, 6255) coupled to a f/4 monochromator (Oriel, MS-257) equipped with a 600 line/mm grating. The output of this light source was modulated using a chopper (Stanford Research Systems, SR-540 at 135 Hz) and focused onto the nc-CdSe nanowire array. The resulting photocurrent was converted to a voltage, amplified (Keithley 428-PROG), and detected using a dual-phase lock-in amplifier (EG&G, 5210). The photocurrent was normalized by the incident optical power (1.2 mW/cm<sup>2</sup> at 500 nm) measured using a digital power meter (Newport, 815) and a photodiode (Newport, 818-SL).

The temporal response of the photocurrent was measured for 350 nanowire nc-CdSe arrays biased by 2.0 V using a diode-pumped, frequency-doubled Nd:VO<sub>4</sub> laser (532 nm, Syntec, ST-532-ST) as the irradiation source. The output from this laser was reduced in diameter using a microscope objective lens (DIN achromatic 4×/0.10) and mechanically chopped (Stanford Research Systems, SR-540) up to 4 kHz. This light beam was directed onto the nanowire array, and its optical power was adjusted using neutral density filters. The resulting photocurrent was converted to a voltage, amplified (Keithley, 428-PROG), and detected using a digital storage oscilloscope (Tektronix, TDS 1012) triggered by the optical pulses produced by a beam splitter and silicon photodiode (OSI Optoelectronics, UV-100). In parallel, the long-period temporal photoresponse was recorded using a computer-controlled DAQ card (National Instrument, NI USB-6221 BNC) controlled by a Labview program. All the photoresponse measurements were carried out in laboratory air using a Faraday cage to minimize stray electrical noise. Current versus voltage traces were measured using a sourcemeter (Keithley, 2400), and these data were recorded using a computer controlled by a Labview program.

**Acknowledgment.** The authors gratefully acknowledge the financial support of this work by the National Science Foundation (CHE-0956524) and University of California-Irvine, School of Physical Sciences Center for Solar Energy. J.C.H. and M.C. acknowledge funding from the DOE Office of Basic Energy Sciences (DE-FG02-96ER45576). We also express our appreciation to Dr. Chi Chen and Dr. Li-Chung Lai for insightful discussions, to Prof. Ken J. Shea for generously lending us the laser used in these studies, and to Prof. Matt Law for the use of the UV-vis spectrometer used for absorption measurements. All electron microscopy was carried out in the Laboratory for

Electron and X-ray Instrumentation (LEXI) at University of California, Irvine.

## REFERENCES AND NOTES

- Kind, H.; Yan, H.; Messer, B.; Law, M.; Yang, P. Nanowire Ultraviolet Photodetectors and Optical Switches. *Adv. Mater.* **2002**, *14*, 158–160.
- Law, M.; Kind, H.; Messer, B.; Kim, F.; Yang, P. Photochemical Sensing of NO<sub>2</sub> with SnO<sub>2</sub> Nanoribbon Nanosensors at Room Temperature. *Angew. Chem., Int. Ed.* **2002**, *41*, 2405–2408.
- Fan, Z.; Chang, P. C.; Lu, J. G.; Walter, E. C.; Penner, R. M.; Lin, C. H.; Lee, H. P. Photoluminescence and Polarized Photo-detection of Single ZnO Nanowires. *Appl. Phys. Lett.* **2004**, *85*, 6128–6130.
- Zhou, J.; Gu, Y.; Hu, Y.; Mai, W.; Yeh, P.-H.; Bao, G.; Sood, A. K.; Polla, D. L.; Wang, Z. L. Gigantic Enhancement in Response and Reset Time of ZnO UV Nanosensor by Utilizing Schottky Contact and Surface Functionalization. *Appl. Phys. Lett.* **2009**, *94*, 191103.
- Ahn, S.-E.; Ji, H. J.; Kim, K.; Kim, G. T.; Bae, C. H.; Park, S. M.; Kim, Y.-K.; Ha, J. S. Origin of the Slow Photoresponse in an Individual Sol-gel Synthesized ZnO Nanowire. *Appl. Phys. Lett.* **2007**, *90*, 153106.
- Soci, C.; Zhang, A.; Xiang, B.; Dayeh, S. A.; Aplin, D. P. R.; Park, J.; Bao, X. Y.; Lo, Y. H.; Wang, D. ZnO Nanowire UV Photodetectors with High Internal Gain. *Nano Lett.* **2007**, *7*, 1003–1009.
- He, J. H.; Chang, P. H.; Chen, C. Y.; Tsai, K. T. Electrical and Optoelectronic Characterization of a ZnO Nanowire Contacted by Focused-Ion-Beam-Deposited Pt. *Nanotechnology* **2009**, *20*, 135701.
- Prades, J. D.; Jimenez-Diaz, R.; Hernandez-Ramirez, F.; Fernandez-Romero, L.; Andreu, T.; Cirera, A.; Romano-Rodriguez, A.; Cornet, A.; Morante, J. R.; Barth, S.; et al. Toward a Systematic Understanding of Photodetectors Based on Individual Metal Oxide Nanowires. *J. Phys. Chem. C* **2008**, *112*, 14639–14644.
- Li, Y.; Dong, X.; Cheng, C.; Zhou, X.; Zhang, P.; Gao, J.; Zhang, H. Fabrication of ZnO Nanorod Array-Based Photodetector With High Sensitivity to Ultraviolet Light. *Phys. B (Amsterdam, Neth.)* **2009**, *404*, 4282–4285.
- Keem, K.; Kim, H.; Kim, G.-T.; Lee, J. S.; Min, B.; Cho, K.; Sung, M.-Y.; Kim, S. Photocurrent in ZnO Nanowires Grown From Au Electrodes. *Appl. Phys. Lett.* **2004**, *84*, 4376–4378.
- Liu, Z.; Zhang, D.; Han, S.; Li, C.; Tang, T.; Jin, W.; Liu, X.; Lei, B.; Zhou, C. Laser Ablation Synthesis and Electron Transport Studies of Tin Oxide Nanowires. *Adv. Mater.* **2003**, *15*, 1754–1757.
- Lee, J.-S.; Sim, S.-K.; Min, B.; Cho, K.; Kim, S. W.; Kim, S. Structural and Optoelectronic Properties of SnO<sub>2</sub> Nanowires Synthesized From Ball-Milled SnO<sub>2</sub> Powders. *J. Cryst. Growth* **2004**, *267*, 145–149.
- Calarco, R.; Marso, M.; Richter, T.; Aykanat, A. I.; Meijers, R.; v. d. Hart, A.; Stoica, T.; Luth, H. Size-Dependent Photoconductivity in MBE-Grown GaN-Nanowires. *Nano Lett.* **2005**, *5*, 981–984.
- Kang, M.; Lee, J.-S.; Sim, S.-K.; Kim, H.; Min, B.; Cho, K.; Kim, G.-T.; Sung, M.-Y.; Kim, S.; Han, H. S. Photocurrent and Photoluminescence Characteristics of Networked GaN Nanowires. *Jap. J. Appl. Phys.* **2004**, *43*, 6868–6872.
- Han, S.; Jin, W.; Zhang, D.; Tang, T.; Li, C.; Liu, X.; Liu, Z.; Lei, B.; Zhou, C. Photoconduction Studies on GaN Nanowire Transistors Under UV and Polarized UV Illumination. *Chem. Phys. Lett.* **2004**, *389*, 176–180.
- Jie, J. S.; Zhang, W. J.; Jiang, Y.; Meng, X. M.; Li, Y. Q.; Lee, S. T. Photoconductive Characteristics of Single-Crystal CdS Nanoribbons. *Nano Lett.* **2006**, *6*, 1887–1892.
- Gao, T.; Li, Q. H.; Wang, T. H. CdS Nanobelts as Photoconductors. *Appl. Phys. Lett.* **2005**, *86*, 173105.
- Chen, J.; Xue, K.; An, J.; Tsang, S.; Ke, N.; Xu, J.; Li, Q.; Wang, C. Photoelectric Effect and Transport Properties of a Single CdS Nanoribbon. *Ultramicroscopy* **2005**, *105*, 275–280 Proceedings of the Sixth International Conference on Scanning Probe Microscopy, Sensors and Nanostructures.
- Paul, G. S.; Agarwal, P. Persistent Photocurrent and Decay Studies in CdS Nanorods Thin Films. *J. Appl. Phys.* **2009**, *106*, 103705.
- Soci, C.; Zhang, A.; Bao, X.-Y.; Kim, H.; Lo, Y.; Wang, D. Nanowire Photodetectors. *J. Nanosci. Nanotechnol.* **2010**, *10*, 1430–1449.
- Chen, R.-S.; Chen, H.-Y.; Lu, C.-Y.; Chen, K.-H.; Chen, C.-P.; Chen, L.-C.; Yang, Y.-J. Ultrahigh Photocurrent Gain in m-Axial GaN Nanowires. *Appl. Phys. Lett.* **2007**, *91*, 223106.
- Jiang, Y.; Zhang, W. J.; Jie, J. S.; Meng, X. M.; Fan, X.; Lee, S.-T. Photoresponse Properties of CdSe Single-Nanoribbon Photodetectors. *Adv. Funct. Mat.* **2007**, *17*, 1795–1800.
- Melnick, D. Zinc Oxide Photoconduction, An Oxygen Adsorption Process. *J. Chem. Phys.* **1957**, *26*, 1136–1146.
- Wu, C.; Jie, J.; Wang, L.; Yu, Y.; Peng, Q.; Zhang, X.; Cai, J.; Guo, H.; Wu, D.; Jiang, Y. Chlorine-doped n-type CdS Nanowires with Enhanced Photoconductivity. *Nanotechnology* **2010**, *21*, 505203.
- Kung, S. C.; van der Veer, W. E.; Yang, F.; Donavan, K. C.; Penner, R. M. 20 Microsecond Photocurrent Response from Lithographically Patterned Nanocrystalline Cadmium Selenide Nanowires. *Nano Lett.* **2010**, *10*, 1481–1485.
- Menke, E. J.; Thompson, M. A.; Xiang, C.; Yang, L. C.; Penner, R. M. Lithographically Patterned Nanowire Electrodeposition. *Nat. Mat.* **2006**, *5*, 914–919.
- Xiang, C.; Kung, S. C.; Taggart, D. K.; Yang, F.; Thompson, M. A.; Guell, A. G.; Yang, Y.; Penner, R. M. Lithographically Patterned Nanowire Electrodeposition: A Method for Patterning Electrically Continuous Metal Nanowires on Dielectrics. *ACS Nano* **2008**, *2*, 1939–1949.
- Xiang, C.; Yang, Y.; Penner, R. M. Cheating the Diffraction Limit: Electrodeposited Nanowires Patterned by Photolithography. *Chem. Commun.* **2009**, 859–873.
- Svechnic, S.; Shtrum, E.; Savialov, L.; Philippo, A.; Matchina, S.; Klochcov, V. Structure and Photoelectric Properties of Thin CdSe Films. *Thin Solid Films* **1972**, *11*, 33–&.
- Rami, M.; Benamar, E.; Fahoume, M.; Chraibi, F.; Ennaoui, A. Effect of Heat Treatment with CdCl<sub>2</sub> on the Electrodeposited CdTe/CdS Heterojunction. *M.J. Cond. Mater.* **2000**, *3*, 66–70.
- Ringel, S. A.; Smith, A. W.; MacDougal, M. H.; Rohatgi, A. The Effects of CdCl<sub>2</sub> on the Electronic Properties of Molecular-Beam Epitaxially Grown CdTe/CdS Heterojunction Solar Cells. *J. Appl. Phys.* **1991**, *70*, 881–889.
- Birkmire, R. W.; Eser, E. Polycrystalline Thin Film Solar Cells: Present Status and Future Potential. *Ann. Rev. Mat. Res.* **1997**, *27*, 625–653.
- Nair, M. T. S.; Nair, P. K.; Zingaro, R. A.; Meyers, E. A. Enhancement of Photosensitivity in Chemically Deposited CdSe Thin Films by Air Annealing. *J. Appl. Phys.* **1993**, *74*, 1879–1884.
- Yoneda, H.; Ueda, K.-i.; Aikawa, Y.; Baba, K.; Shohata, N. The Grain Size Dependence of the Mobility and Lifetime in Chemical Vapor Deposited Diamond Photoconductive Switches. *J. Appl. Phys.* **1998**, *83*, 1730–1734.
- Chakrabarti, R.; Dutta, J.; Maity, A.; Chaudhuri, S.; Pal, A. Photoconductivity of CdTe films. *Thin Solid Films* **1996**, *288*, 32–35.
- Ghosh, R.; Mallik, B.; Basak, D. Dependence of Photoconductivity on the Crystallite Orientations and Porosity of Polycrystalline ZnO Films. *Appl. Phys. A: Mat. Sci. Proc.* **2005**, *81*, 1281–1284.
- Klein, J. D.; Herrick, R. D.; Palmer, D.; Sailor, M. J.; Brunlik, C. J.; Martin, C. R. Electrochemical Fabrication of Cadmium Chalcogenide Microdiode Arrays. *Chem. Mater.* **1993**, *5*, 902–904.
- Kressin, A. M.; Doan, V. V.; Klein, J. D.; Sailor, M. J. Synthesis of Stoichiometric Cadmium Selenide Films via Sequential Monolayer Electrodeposition. *Chem. Mater.* **1991**, *3*, 1015–1020.
- Li, Q.; Brown, M. A.; Hemminger, J. C.; Penner, R. M. Luminescent Polycrystalline Cadmium Selenide Nanowires Synthesized by Cyclic Electrodeposition/Stripping Coupled with Step Edge Decoration. *Chem. Mater.* **2006**, *18*, 3432–3441.

40. Menke, E. J.; Brown, M. A.; Li, Q.; Hemminger, J. C.; Penner, R. M. Bismuth Telluride ( $\text{Bi}_2\text{Te}_3$ ) Nanowires: Synthesis by Cyclic Electrodeposition/Stripping, Thinning by Electrooxidation, and Electrical Power Generation. *Langmuir* **2006**, *22*, 10564–10574.
41. Schierhorn, M.; Boettcher, S. W.; Ivanovskaya, A.; Norvell, E.; Sherman, J. B.; Stucky, G. D.; Moskovits, M. Fabrication and Electrochemical Photovoltaic Response of CdSe Nanorod Arrays. *J. Phys. Chem. C* **2008**, *112*, 8516–8520.
42. Peña, D. J.; Mbindyo, J. K. N.; Carado, A. J.; Mallouk, T. E.; Keating, C. D.; Razavi, B.; Mayer, T. S. Template Growth of Photoconductive Metal-CdSe-Metal Nanowires. *J. Phys. Chem. B* **2002**, *106*, 7458–7462.
43. Carpenter, D. T.; Rickman, J. M.; Barmak, K. A Methodology for Automated Quantitative Microstructural Analysis of Transmission Electron Micrographs. *J. Appl. Phys.* **1998**, *84*, 5843–5854.
44. Patterson, A. L. The Scherrer Formula for X-Ray Particle Size Determination. *Phys. Rev.* **1939**, *56*, 978–982.
45. Bandaranayake, R. J.; Wen, G. W.; Lin, J. Y.; Jiang, H. X.; Sorensen, C. M. Structural Phase Behavior in II–VI Semiconductor Nanoparticles. *Appl. Phys. Lett.* **1995**, *67*, 831–833.
46. Kale, R. B.; Lokhande, C. D. Systematic Study on Structural Phase Behavior of CdSe Thin Films. *J. Phys. Chem. B* **2005**, *109*, 20288–20294.
47. Kale, R. B.; Lokhande, C. D. Band Gap Shift, Structural Characterization and Phase Transformation of CdSe Thin Films From Nanocrystalline Cubic to Nanorod Hexagonal on Air Annealing. *Semicond. Sci. Technol.* **2005**, *20*, 1–9.
48. Portillo-Moreno, O.; Lozada-Morales, R.; Rubn-Falfán, M.; Pérez-Álvarez, J. A.; Zelaya-Angel, O.; Baños-López, L. Phase Transformation on CdSe Thin Films Under Annealing in Ar+ $\text{Se}_2$  Atmosphere. *J. Phys. Chem. Solids* **2000**, *61*, 1751–1754.
49. Farva, U.; Park, C. Influence of Thermal Annealing on the Structural and Optical Properties of CdSe Nanoparticles. *Sol. Energy Mater.* **2010**, *94*, 303–309.
50. Gaarenstroom, S.; Winograd, N. Initial and Final State Effects in ESCA Spectra of Cadmium and Silver Oxides. *J. Chem. Phys.* **1977**, *67*, 3500–3506.
51. Polak, M. X-Ray Photoelectron Spectroscopic Studies of  $\text{CdSe}_{0.65}\text{Te}_{0.35}$ . *J. Electron Spectrosc. Relat. Phenom.* **1982**, *28*, 171–176.
52. Agostinelli, E.; Battistoni, C.; Fiorani, D.; Mattogno, G. An XPS Study of the Electronic Structure of the  $\text{Zn}_x\text{Cd}_{1-x}\text{Cr}_2\text{S}_4$  and  $\text{Zn}_x\text{Cd}_{1-x}\text{Cr}_2\text{Se}_4$  Spinel System. *J. Phys. Chem. Solids* **1989**, *50*, 269–272.
53. Wagner, C. D.; Naumkin, A. V.; Kraut-Vass, A.; Allison, J. W.; Powell, C. J.; Rumble, J. R., Jr. *NIST X-ray Photoelectron Spectroscopy Database*.
54. Seals, R.; Alexande, R.; Taylor, L.; Dillard, J. Core Electron Binding-Energy Study of Group IIB-VIIA Compounds. *Inorg. Chem.* **1973**, *12*, 2485–2487.
55. Jie, J. S.; Zhang, W. J.; Jiang, Y.; Lee, S. T. Single-Crystal CdSe Nanoribbon Field-Effect Transistors and Photoelectric Applications. *Appl. Phys. Lett.* **2006**, *89*, 133118.
56. Amalnerkar, D. P. Photoconducting and Allied Properties of CdS Thick Films. *Mater. Chem. Phys.* **1999**, *60*, 1–21.
57. Sze, S. M.; Ng, K. K. *Physics of Semiconductor Devices*, 3rd ed.; Wiley & Sons: NJ, 2007.
58. Rosenthaler, E.; Vinter, B. *Optoelectronics*; Cambridge University Press: Cambridge, UK, 2002.
59. Kazmerski, L.; Berry, W.; Allen, C. Role of Defects in Determining the Electrical Properties of CdS Thin Films. I. Grain Boundaries and Surfaces. *J. Appl. Phys.* **1972**, *43*, 3515–3521.
60. Seto, J. Electrical Properties of Polycrystalline Silicon Films. *J. Appl. Phys.* **1975**, *46*, 5247–5254.
61. Rose, A. *Concepts in Photoconductivity and Allied Problems*; Interscience Publishers: New York, 1963; Vol. 19.
62. Bube, R. H. *Photoelectronic Properties of Semiconductors*; Cambridge University Press: Cambridge, 1992.
63. Bube, R.; Grove, W.; Murchison, R. Photoconductivity Decay in Imperfect Crystals. *J. Appl. Phys.* **1967**, *38*, 3515–.
64. Fan, Z.; Ho, J. C.; Jacobson, Z. A.; Razavi, H.; Javey, A. Large-scale, Heterogeneous Integration of Nanowire Arrays for Image Sensor Circuitry. *Proc. Natl. Acad. Sci.* **2008**, *105*, 11066–11070.
65. Wang, X.; Wang, J.; Zhou, M.; Zhu, H.; Wang, H.; Cui, X.; Xiao, X.; Li, Q. CdTe Nanorod Arrays on ITO: From Microstructure to Photoelectrical Property. *J. Phys. Chem. C* **2009**, *113*, 16951–16953.
66. Joshi, N. V. *Photoconductivity: Art, Science, and Technology*; M. Dekker: New York, 1990; Vol. 25.
67. Yang, Y.; Taggart, D. K.; Brown, M. A.; Xiang, C.; Kung, S.-C.; Yang, F.; Hemminger, J. C.; Penner, R. M. Wafer-Scale Patterning of Lead Telluride Nanowires: Structure, Characterization, and Electrical Properties. *ACS Nano* **2009**, *3*, 4144–4154.
68. Yang, Y.; Kung, S. C.; Taggart, D. K.; Xiang, C.; Yang, F.; Brown, M. A.; Guell, A. G.; Kruse, T. J.; Hemminger, J. C.; Penner, R. M. Synthesis of PbTe Nanowire Arrays using Lithographically Patterned Nanowire Electrodeposition. *Nano Lett.* **2008**, *8*, 2447–2449.
69. Ndiaye, A.; Youm, I. Effects of Post-Deposition Processing on Microstructural Properties of Cadmium Selenide Thin Films Grown from Solution. *Eur. Phys. J. Appl. Phys.* **2003**, *23*, 75–82.